PHYSICAL REVIEW LETTERS **126,** 137403 (2021)

Quantum Interference Visibility Spectroscopy in Two-Color Photoemission from Tungsten Needle Tips

Ang Li,[1,*] Yiming Pan,[2] Philip Dienstbier,[1] and Peter Hommelhoff[1,†]
[1] *Department of Physics, Friedrich-Alexander Universität Erlangen-Nürnberg (FAU), Staudtstraße 1, 91058 Erlangen, Germany*
[2] *Physics Department and Solid State Institute, Technion, Haifa 32000, Israel*

(Received 26 October 2020; accepted 4 February 2021; published 2 April 2021)

When two-color femtosecond laser pulses interact with matter, electrons can be emitted through various multiphoton excitation pathways. Quantum interference between these pathways gives rise to a strong oscillation of the photoemitted electron current, experimentally characterized by its visibility. In this Letter, we demonstrate the two-color visibility spectroscopy of multiphoton photoemissions from a solid-state nanoemitter. We investigate the quantum pathway interference visibility over an almost octave-spanning wavelength range of the fundamental (ω) femtosecond laser pulses and their second harmonic (2ω). The photoemissions show a high visibility of $90\% \pm 5\%$, with a remarkably constant distribution. Furthermore, by varying the relative intensity ratio of the two colors, we find that we can vary the visibility between 0% and close to 100%. A simple but highly insightful theoretical model allows us to explain all observations, with excellent quantitative agreements. We expect this work to be universal to all kinds of photo-driven quantum interference, including quantum control in physics, chemistry, and quantum engineering.

DOI: 10.1103/PhysRevLett.126.137403

Manipulating atomic and molecular processes using coherent light lies at the core of quantum control. It can be achieved by tuning quantum interference between two competing pathways by varying the relative phase and amplitudes of bichromatic laser fields, driving the relevant transitions. The resulting quantum mechanical pathway interference influences the yield of the final states [1–5]. This was first observed in the actively controlled photodissociation of molecules [6–8]. Later, this method was extended to the ionization of atoms, where the energy and angular distributions of emitted electrons were manipulated by tuning the laser parameters [9–13]. Also, the coherent control of atomic phenomena has been reported in autoionization [14–16] and dissociative ionization [17–20]. Using the second laser field to introduce asymmetry enables the study of the manipulation of high harmonic generation [21–23], the making of ultracold molecules [24], the measurement and control of tunneling processes [25,26], plasmonic field distribution [27], and photoelectron holography [28].

This control scheme was also applied to metallic nanoemitters. Photoemissions from the surface of metallic needle tips driven by two-color femtosecond laser fields have shown a remarkably large coherence, indicated by a visibility reaching 97.5% [29–33]. These photoemissions displayed a homogeneous modulation for all emitted electron energies driven with a two-color frequency pair of a fundamental and second harmonic ($\omega, 2\omega$). Here, we demonstrate the "visibility spectroscopy" of multiphoton photoemissions, i.e., the visibility of the coherent signal is investigated in terms of the relative phase, intensities, and frequencies of the two laser fields (ω, 2ω). We find that, over an almost octave-spanning range of tuned wavelengths, the visibility shows a nearly constant value on the level of $90\% \pm 5\%$. We propose a quantum pathway model that attributes the robust interference to an exact substitution of one (2ω) photon for two ω photons from two competing pathways. Furthermore, this model explains the observed intensity scaling and visibility with excellent quantitative agreement over the entire parameter space.

Our experimental setup is schematically depicted in Fig. 1(a). Ultrashort ~67 fs laser pulses at the (angular) center frequency ω and their second-harmonic pulses at 2ω are focused onto a [110]-oriented tungsten needle tip that is

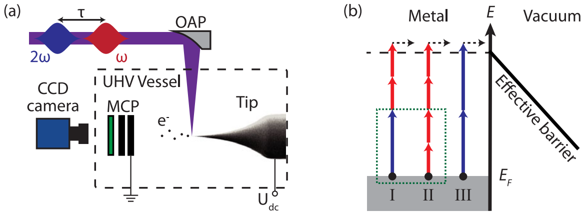

FIG. 1. Experimental setup and multiphoton absorption in a metallic needle tip. (a) Femtosecond laser pulses (ω) and their second harmonic (2ω) are focused onto a tungsten needle tip with an off-axis parabola (OAP). Photoelectrons from the tip biased with U_{dc} are detected on an MCP with a phosphor screen and are imaged on a CCD camera. (b) Schematic energy diagram of photoemission processes through three pathways (I, II, III). The green dotted frame marks the substitution of one (2ω) photon for two ω photons in the absorption pathways.

etched electrochemically from a tungsten wire to a sharp tip. Field ion microscopy yields a tip apex radius of (14 ± 1) nm [34]. The second-harmonic pulses are phase stable relative to the fundamental pulses due to the parametric 2ω generation process, and they are temporally delayed by a variable time delay τ. The two-color laser pulses are focused on the tip with a 152 mm effective focal length, 90° off-axis parabolic mirror situated outside of the ultrahigh vacuum (UHV) vessel. Inside the UHV vessel, photoelectrons from the needle tip are detected by a microchannel plate (MCP) detector with a phosphor screen, which is imaged by a CCD camera.

The multiphoton processes at the surface of the needle tip driven by the two-color laser field are schematically presented in Fig. 1(b). Electrons inside the metal surface of the needle tip can be excited to an energy of $E_F + 4\hbar\omega$ through three photon-induced pathways to overcome the effective barrier. Interference between all three pathways shown should, in theory, be observed, resulting in photoemission oscillations depending on the relative phase between the ω and 2ω pulses. Particularly, a substitution of one (2ω) photon for two ω photons from the interfering pathways I and II [green dotted frame in Fig. 1(b)] should lead to an oscillation with a frequency of 2ω, whereas the interference between pathways II and III should result in the doubled oscillation frequency of 4ω [1]. We note that we observe oscillations with 2ω only; thus, we may neglect the interference between pathways II and III, as shown and discussed below. Furthermore, interference between pathways I and III is essentially equivalent to the interference between pathways I and II since both of them feature the substitution of one (2ω) photon for two ω photons. Hence, the following discussion is focused on the interference between pathways I and II.

We observe strong oscillations of the photocurrent depending on the time delay τ when the ω and 2ω pulses are close to a perfect temporal overlap (insets of Fig. 2). These oscillations of the photocurrent can be well fitted by sinusoidal functions (red solid lines). The frequency of the oscillation obtained from the fitted sinusoidal functions and from the Fourier transform of the measured data corresponds to the second-harmonic frequency 2ω to within 4%, whereas the 4ω component is not visible and is suppressed by at least −12.1 dB. From the sinusoids, we obtain the visibility of the photocurrent oscillations, defined as

$$V = \frac{N_{\max} - N_{\min}}{N_{\max} + N_{\min}}, \tag{1}$$

where $N_{\max}$ corresponds to the maximum and $N_{\min}$ to the minimum of the sinusoid. The visibilities of these oscillating photocurrents as a function of wavelength are presented in Fig. 2. They reach up to 96% at the wavelength pairs (1210 nm and 605 nm) and (1460 nm and 730 nm). Clearly, at each wavelength pair within the large wavelength range investigated (from 1180 nm to 2000 nm in steps of 10 nm), we observe strong oscillations in the photocurrent. Significantly, a nearly constant distribution of the visibility with an average of 90% ± 5% is observed. Within the measured wavelength range, the visibilities are always larger than 72%, indicating a robust and wavelength-independent interference process.

To obtain a single data point in Fig. 2, we have recorded short ω-2ω delay spectra as shown in the insets of Fig. 2. We have chosen intensities such that we always operate under stable conditions. The plotted visibilities are achieved by setting I_ω and varying $I_{2\omega}$ to obtain the maximum visibility. We find that the maximum visibility intensity ratio $I_{2\omega}/I_\omega$ equals $93\% \pm 31\%$ for all data points at an incident fundamental intensity of $(7.0 \pm 1.1) \times 10^{10}\ \mathrm{W\,cm^{-2}}$.

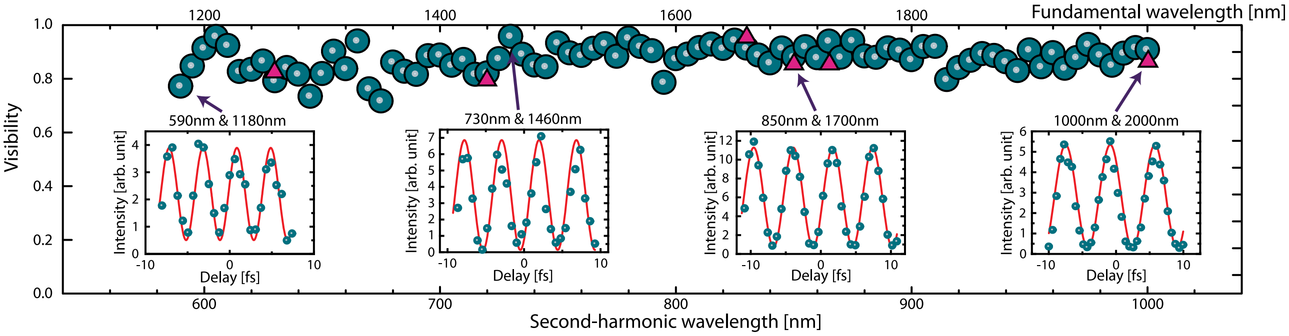

FIG. 2. Visibility of the two-color coherent control in multiphoton photoemissions. The visibilities of the photocurrent oscillations are plotted as a function of the corresponding second-harmonic wavelength of the applied wavelength pairs, which are varied from 590 nm (2ω) and 1180 nm (ω) to 1000 nm (2ω) and 2000 nm (ω). A high visibility of 90% ± 5% with a roughly constant distribution is found. The visibilities calculated from the theory [Eq. (5)] are shown as pink triangles. Insets: Typical photocurrent oscillations when the needle tip is illuminated by the two-color laser field. Photocurrent intensities detected on the MCP detector screen are shown depending on the time delay τ between ω and 2ω pulses. Sine fits to the data are displayed as red solid lines, clearly revealing an oscillation frequency of 2ω.

To elucidate the underlying physical process, we propose a simple yet insightful theoretical model based on multiphoton absorption physics from the metal needle tip. We assume that the interaction between the bound electron inside of the metal and the laser field can be described by the Hamiltonian $H_{\mathrm{int}} = -(p \cdot A)e/m$ in the minimal coupling approximation, with electron charge e, effective mass m, momentum p, and vector potential A describing the nearfield-enhanced laser field. Here, the metallic ground state is filled by Bloch electrons with energy E beneath the Fermi energy E_F. The initial electronic state, therefore, takes the form $|\Phi_i(t)\rangle = \exp(-iEt/\hbar)|k\rangle$ with the electron wave number $k \leq k_F$ (Fermi wave number). The enhanced laser field is approximately given by $A = g_\omega F \sin(\omega t + \phi_0)$, where $g_\omega = -\xi_\omega/\omega$ depends on the dimensionless field enhancement factor ξ_ω, which can be determined through numerical simulations [35]. The parameter F is the amplitude of the incident laser electric field, and $\phi_0 = \phi_\omega - \phi_e$ is the phase difference between the laser pulse (ϕ_ω) and the phase of the Bloch electron (ϕ_e).

By solving the time-dependent Schrödinger equation in the interaction picture, we obtain the final state of the electron after the interaction,

$$|\Phi_f(t)\rangle = \sum_{n=-\infty}^{\infty} J_n\left(\frac{ek\Delta t g_\omega}{m}F\right) e^{\mathrm{in}(\omega t+\phi_0)}|\Phi_i(t)\rangle, \quad (2)$$

where J_n are the nth-order Bessel functions of the first kind, and n corresponds to the order of the multiphoton process. Specifically, the order n takes integer values ($n = 0, \pm 1, \pm 2 \ldots$), denoting photon absorption ($n < 0$) and photon emission ($n > 0$) with a photon energy of $\hbar\omega$. Δt is the duration of the interaction between the electron and the enhanced laser field, which is approximated as $\Delta t \approx 200$ as based on the length scale (few angstroms [36]) of the interaction region between the screened electromagnetic field and the Bloch electron with Fermi velocity v_F extending into vacuum. The dimensionless argument of the Bessel function describes the effective exchanged photon number $\eta_\omega = (ek\Delta t g_\omega/m)F$. For the multiphoton photoemission process through pathways I and II in Fig. 1(b), the final electronic state is composed of the terms $J_{-1}(\eta_{2\omega})e^{-i(2\omega t+\phi_{2\omega}-\phi_{\mathrm{e}})}$, $J_{-2}(\eta_\omega)e^{-2i(\omega t+\phi_\omega-\phi_{\mathrm{e}})}$, and $J_{-4}(\eta_\omega)e^{-4i(\omega t+\phi_\omega-\phi_{\mathrm{e}})}$. The resultant final state population via pathways I and II then reads

$$\begin{aligned}|\Phi_f(\omega, 2\omega)|^2 = {} & |J_{-4}(\eta_\omega)|^2 + |J_{-1}(\eta_{2\omega})J_{-2}(\eta_\omega)|^2 \\ & + 2|J_{-4}(\eta_\omega)J_{-1}(\eta_{2\omega})J_{-2}(\eta_\omega)| \\ & \times \cos(\phi_{2\omega} - 2\phi_\omega + \phi_e), \end{aligned} \quad (3)$$

where the first two terms denote the contributions from pathways I and II separately, and the third term describes the interference between the pathways oscillating with the relative phase $\phi_{2\omega} - 2\phi_\omega + \phi_e$. Using the asymptotic form of the Bessel function of the nth order $J_n(\eta_\omega) = (-2)^n/(-n! \cdot \eta_\omega^n)$, Eq. (3) can be calculated explicitly. Together with Eq. (1), we obtain the visibility as

$$V = \frac{2\alpha I_\omega \sqrt{\beta I_{2\omega}}}{\alpha^2 I_\omega^2 + \beta I_{2\omega}}, \quad (4)$$

$$= \frac{2\sqrt{\Gamma\tilde{I}}}{1 + \Gamma\tilde{I}}, \quad (5)$$

where α and β are the proportionality factors for the absorption of ω and 2ω photons, respectively. By substituting $\beta I_{2\omega}/\alpha^2 I_\omega^2$ with $\Gamma\tilde{I}$, the expression of the visibility in Eq. (4) is reduced to a simple equation [Eq. (5)]. The dimensionless product $\Gamma\tilde{I}$ describes the branching ratio between the two sub-pathways in I and II. This ratio fully controls the visibility of the quantum pathway interference independent of the total photon absorption number n. A visibility of 100% will occur if the two sub-pathways contribute equally, i.e., $\Gamma\tilde{I} = 1$. Further, we deduce that the visibility can be tuned by variation of the intensity branching ratio $\tilde{I} = I_{2\omega}/I_\omega^2$ or the material branching ratio $\Gamma = \beta/\alpha^2$, which is related to the optical response of the material.

Figs. 3(a)–3(c) show a measurement of the visibility scaling as a function of the intensity branching ratio $\tilde{I}$ for three wavelength pairs. The fundamental intensities are as different as $I_{1440\,\mathrm{nm}} = 9.4 \times 10^{10}\ \mathrm{W\,cm^{-2}}$, $I_{1560\,\mathrm{nm}} = 6.7 \times 10^9\ \mathrm{W\,cm^{-2}}$, and $I_{1700\,\mathrm{nm}} = 8.0 \times 10^{10}\ \mathrm{W\,cm^{-2}}$. Red solid lines in Figs. 3(a)–3(c) are the curves fitted by Eq. (5). Although the measured visibilities follow rather rapid [Figs. 3(b) and 3(c)] or more gentle scaling behaviors [Fig. 3(a)], the analytical expression of the visibility agrees well with all three measurements, confirming the theoretically deduced visibility behavior.

The material branching ratio Γ, which jointly controls the visibility with $\tilde{I}$, can be derived with the effective exchanged photon number $\eta_\omega = ek\Delta t g_\omega F/m$ as

$$\Gamma = \frac{\beta}{\alpha^2} = \frac{72 m^2 \epsilon_0 c}{e^2 k_F^2 \Delta t^2} \cdot \frac{\omega^2 \xi_{2\omega}^2}{\xi_\omega^4}, \quad (6)$$

where m is the electron mass, ϵ_0 is the vacuum permittivity, c is the speed of light in vacuum, and $k_F = \sqrt{2mE_F}/\hbar = 1.4 \times 10^{10}\ \mathrm{m^{-1}}$ is the Fermi wave number [37]. The field enhancement factors $\xi_{\omega,2\omega}$ are determined by a finite difference time domain simulation for the different wavelengths. This way we can calculate Γ (see the Supplemental Material for details [38]) and hence obtain the visibilities for different wavelengths from the model (pink triangles in Fig. 2).

The visibilities determined with the calculated Γ are shown as blue solid lines in Figs. 3(a)–3(c). The blue

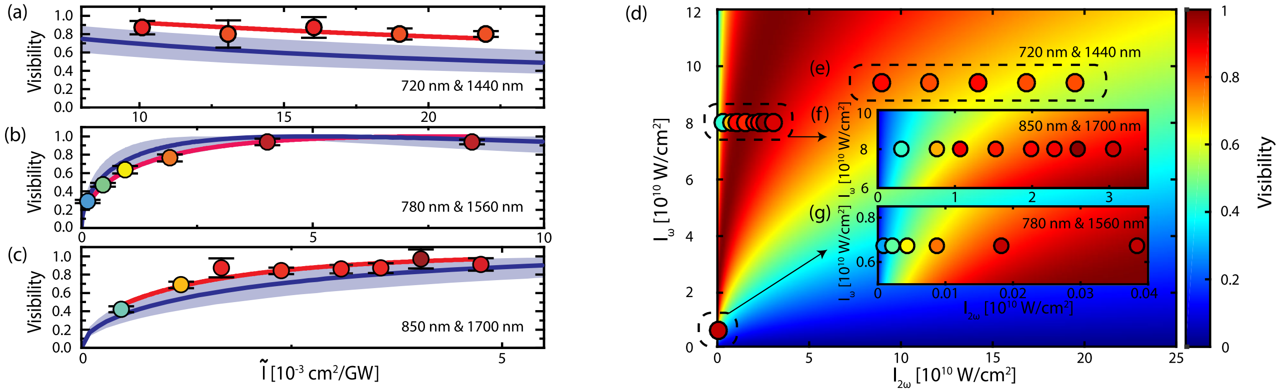

FIG. 3. Comparison of theory and observations of the visibility scaling as a function of the laser intensities. (a)–(c) Visibility scaling depending on the intensity branching ratio $\tilde{I} = I_{2\omega}/I_{\omega}^2$, measured by varying the second-harmonic intensity $I_{2\omega}$. The data in (b) are taken from [29]. The color coding of the circles also represents the measured visibilities corresponding to the color bar in (d). Red solid lines in (a)–(c) depict fit curves using Eq. (5), whereas the blue solid lines show the calculated visibility using Eqs. (5) and (6). The blue band indicates the uncertainty of the calculated visibility obtained from the 10% uncertainty assumed in the field enhancement factors. (d) The calculated visibility as a function of fundamental intensity I_ω and second-harmonic intensity $I_{2\omega}$ using Eq. (4) for the wavelength pair of 720 nm and 1440 nm (color map). The measured visibilities of (a)–(c) are plotted as colored circles in (d) (black dashed frames) as well as in (f) and (g). (e) The data points show a consistently larger visibility and hence deviate from the theory color map (background color) as they do in (a). (f), (g) Two enlarged insets for better visualization where the background color in (f) is calculated for 850 nm and 1700 nm, while the background color in (g) is calculated for 780 nm and 1560 nm, with experimental data points (colored circles) that are the same as shown in (b) and (c). We note the excellent agreement of the experimentally measured visibility (circles) and the theoretical visibility (background color).

shadowed areas depict the uncertainty of the visibility due to an assumed uncertainty of the simulated field enhancement factors of 10%. These results, obtained solely from our model, are also in good agreement with the experimental results and further confirm the visibility tuning, also with Γ. Thus, the branching ratio $\Gamma\tilde{I}$, implying the substitution of one (2ω) photon for two ω photons, fully characterizes the visibility [Eq. (5)].

The visibility is also determined via Eq. (4) with the calculated proportionality factors α and β as a function of the incident laser intensities I_ω and $I_{2\omega}$. The resulting visibility distribution is shown as the background color maps of Figs. 3(d), 3(f), and 3(g) for the wavelength pairs presented in (a), (c), and (b), respectively. In (d), the calculated value of the proportionality factors $\alpha = 3.15 \times 10^{-12}\ \mathrm{cm^2\,W^{-1}}$ and $\beta = 6.09 \times 10^{-12}\ \mathrm{cm^2\,W^{-1}}$ for 1440 nm and 720 nm are adapted. Clearly, we find a large high-visibility area ($V \geq 90\%$) with an increasing fundamental intensity I_ω, which is also in agreement with previous theoretical work [32]. This elegantly explains the large differences in the scaling behavior presented in (a)–(c). These measurements are conducted with different levels of I_ω. In most regions, $\Gamma\tilde{I} \gg 1$, hence from Eq. (5), $V \propto \sqrt{\tilde{I}} \propto I_\omega^{-1} I_{2\omega}^{1/2}$. Thus, to keep V constant, $I_{2\omega}$ needs to scale quadratically with I_ω. This notion becomes obvious when insets (f) and (g) are compared: $I_{2\omega}$ for the maximum visibility is approximately $167 = 12.9^2$ times larger in (f) as in (g), whereas the I_ω is 12 (≈ 12.9) times larger, confirming the V scaling behavior. We note that the range of high visibility may become smaller when the field of the fundamental laser field is entering the strong-field regime [32].

In addition, at an appropriate fundamental intensity I_ω, a broad range of $I_{2\omega}$ is expected to yield a high visibility. For the second-harmonic intensity ratio $I_{2\omega}/I_\omega = 93\% \pm 31\%$ with $I_\omega = (7.0 \pm 1.1) \times 10^{10}\ \mathrm{W\,cm^{-2}}$ employed in Fig. 2, an average visibility of 87% with a deviation as small as 7% is predicted by Eq. (4), which is in great accordance with the measured visibility of 90% ± 5%. Conversely, for the fundamental intensity $I_\omega = (7.0 \pm 1.1)10^{10}\ \mathrm{W\,cm^{-2}}$ used in the experiment, an extensive range of the second-harmonic intensity ratios from 12% to 77% is predicted to obtain the measured average visibility of 90%, which is also consistent with the experiment. This further explains the almost constant distribution of the visibilities measured against a wide spectrum of wavelengths and laser intensity ratios. These additional agreements further support the proposed model, which not only fully explains the observed features in the experimental results but also provides new insight and further degrees of control in quantum pathway interference.

Up to this point, the discussion was based on an estimated interaction duration $\Delta t = 200$ as resulting from the duration of the Bloch electron, with the Fermi velocity $v_F = 1.6 \times 10^6\ \mathrm{m\,s^{-1}}$ for tungsten [37], traversing the screening length inside the metal and the Bloch wave extension in the vacuum (~3 Å [36]). This estimation holds for any laser frequency as long as the fundamental frequency is lower than the plasma frequency of the material (otherwise the screening length becomes much larger) [39]. Furthermore, we expect this estimation to also hold for atoms where the extension of the wave function in vacuum dominates the interaction duration Δt, which can be varied by changing the height of the ionization potential. Additionally, the field enhancement factors are determined experimentally in another ongoing work [40], where the field enhancement factors are directly evaluated from the scaling of the cutoff energy in strong-field electron energy spectra. The experimentally obtained field enhancement factors $\xi_{1560\ \mathrm{nm}} = 5.5 \pm 0.8$ and $\xi_{780\ \mathrm{nm}} = 2.8 \pm 0.4$, together with $\Gamma_{780\ \mathrm{nm}} = 1.3 \times 10^{11}\ \mathrm{W\,cm^{-2}}$ from the fit curve in Fig. 3(c), yield a duration of (570 ± 172) as from Eq. (6). This lies quantitatively in the same range as the estimated duration. Hence, conversely, using measured field enhancement factors for different wavelengths, we should be able to estimate the interaction duration for each wavelength from Eq. (6) in future work.

In conclusion, we have demonstrated the visibility spectroscopy of quantum pathway interference in multiphoton photoemissions at a tungsten needle tip driven by two-color laser fields. A roughly constant visibility of 90% ± 5% over an almost octave-spanning fundamental laser wavelength range from 1180 nm to 2000 nm was observed, suggesting a universal quantum pathway interference. This observation is well explained by the proposed theoretical model, which strongly supports the coherent emission physics to be strictly limited to the replacement of two fundamental photons with one second-harmonic photon despite various other possible processes. Furthermore, the reported visibility scaling with respect to the laser intensity ratio is perfectly matched by our model. We expect this fundamental quantum path interference model to hold as long as the fundamental frequency is lower than the plasma frequency of the material, and at least two fundamental photons are required to drive photoemission. Even more importantly, we expect this model to be applicable to virtually any driving frequency and any material. In particular, we envision that two-color visibility spectroscopy will offer a powerful tool for gaining deep insights in multiphoton processes and photoemission dynamics in materials as different as individual atoms, molecules, clusters, and nanomaterials, as well as extended surfaces. Examples include access to the quantum phases of the electronic states involved, the identification of resonant intermediate states, and the measurement of decoherence effects due to environmental couplings (see the Supplemental Material for more details).

The authors thank Michael Krüger for insightful discussion. This work was funded by the Gordon and Betty Moore Foundation (GBMF) through Grant No. GBMF4744 "Accelerator on a Chip International Program-ACHIP," BMBF via 05K16WEC and 05K16RDB, ERC Grants "Near Field Atto" and "AccelOnChip," DFG SPP 1840, and DFG SFB 953.

[*]Corresponding author.
ang.li@fau.de
[†]Corresponding author.
peter.hommelhoff@fau.de

[1] M. Shapiro and P. Brumer, *Quantum Control of Molecular Processes* (Wiley-VCH Verlag GmbH & Co. KGaA, Weinheim, Germany, 2011).

[2] M. Shapiro and P. Brumer, Laser control of product quantum state populations in unimolecular reactions, J. Chem. Phys. **84**, 4103 (1986).

[3] P. Brumer and M. Shapiro, Control of unimolecular reactions using coherent light, Chem. Phys. Lett. **126**, 541 (1986).

[4] M. Shapiro, J. W. Hepburn, and P. Brumer, Simplified laser control of unimolecular reactions: Simultaneous (ω_1, ω_3) excitation, Chem. Phys. Lett. **149**, 451 (1988).

[5] C. K. Chan, P. Brumer, and M. Shapiro, Coherent radiative control of IBr photodissociation via simultaneous (ω_1, ω_3) excitation, J. Chem. Phys. **94**, 2688 (1991).

[6] S.-P. Lu, S. M. Park, Y. Xie, and R. J. Gordon, Coherent laser control of bound-to-bound transitions of HCl and CO, J. Chem. Phys. **96**, 6613 (1992).

[7] L. Zhu, V. Kleiman, X. Li, S. P. Lu, K. Trentelman, and R. J. Gordon, Coherent laser control of the product distribution obtained in the photoexcitation of HI, Science **270**, 77 (1995).

[8] E. Charron, A. Giusti-Suzor, and F. H. Meis, Coherent control of photodissociation in intense laser fields, J. Chem. Phys. **103**, 7359 (1995).

[9] C. Chen, Y.-Y. Yin, and D. S. Elliott, Interference Between Optical Transitions, Phys. Rev. Lett. **64**, 507 (1990).

[10] C. K. Chan, P. Brumer, and M. Shapiro, Interference Between Optical Transitions and Control of Relative Cross Sections, Phys. Rev. Lett. **64**, 3199 (1990).

[11] H. G. Muller, P. H. Bucksbaum, D. W. Schumacher, and A. Zavriyev, Above-threshold ionisation with a two-colour laser field, J. Phys. B **23**, 2761 (1990).

[12] D. W. Schumacher, F. Weihe, H. G. Muller, and P. H. Bucksbaum, Phase Dependence of Intense Field Ionization: A Study Using Two Colors, Phys. Rev. Lett. **73**, 1344 (1994).

[13] F. Ehlotzky, Atomic phenomena in bichromatic laser fields, Phys. Rep. **345**, 175 (2001).

[14] T. Nakajima and P. Lambropoulos, Manipulation of the Line Shape and Final Products of Autoionization Through the Phase of the Electric Fields, Phys. Rev. Lett. **70**, 1081 (1993).

[15] T. Nakajima and P. Lambropoulos, Effects of the phase of a laser field on autoionization, Phys. Rev. A **50**, 595 (1994).

[16] D. Xenakis, N. E. Karapanagioti, O. Faucher, E. Hertz, and D. Charalambidis, Observation of field phase dependent autoionization, J. Phys. B **32**, 341 (1999).

[17] B. Sheehy, B. Walker, and L. F. DiMauro, Phase Control in the Two-Color Photodissociation of HD^+, Phys. Rev. Lett. **74**, 4799 (1995).

[18] M. R. Thompson, M. K. Thomas, P. F. Taday, J. H. Posthumus, A. J. Langley, L. J. Frasinski, and K. Codling, One and two-colour studies of the dissociative ionization and Coulomb explosion of H_2 with intense Ti:sapphire laser pulses, J. Phys. B **30**, 5755 (1997).

[19] A. D. Bandrauk, S. Chelkowski, and N. H. Shon, Measuring the Electric Field of Few-Cycle Laser Pulses by Attosecond Cross Correlation, Phys. Rev. Lett. **89**, 283903 (2002).

[20] H. Ohmura, T. Nakanaga, and M. Tachiya, Coherent Control of Photofragment Separation in the Dissociative Ionization of IBr, Phys. Rev. Lett. **92**, 113002 (2004).

[21] I. J. Kim, C. M. Kim, H. T. Kim, G. H. Lee, Y. S. Lee, J. Y. Park, D. J. Cho, and C. H. Nam, Highly Efficient High-Harmonic Generation in an Orthogonally Polarized Two-Color Laser Field, Phys. Rev. Lett. **94**, 243901 (2005).

[22] J. Mauritsson, P. Johnsson, E. Gustafsson, A. L'Huillier, K. J. Schafer, and M. B. Gaarde, Attosecond Pulse Trains Generated Using Two Color Laser Fields, Phys. Rev. Lett. **97**, 013001 (2006).

[23] L. Brugnera, D. J. Hoffmann, T. Siegel, F. Frank, A. Zaïr, J. W. G. Tisch, and J. P. Marangos, Trajectory Selection in High Harmonic Generation by Controlling the Phase between Orthogonal Two-Color Fields, Phys. Rev. Lett. **107**, 153902 (2011).

[24] C. P. Koch, E. Luc-Koenig, and F. Masnou-Seeuws, Making ultracold molecules in a two-color pump-dump photoassociation scheme using chirped pulses, Phys. Rev. A **73**, 033408 (2006).

[25] N. Dudovich, O. Smirnova, J. Levesque, Y. Mairesse, M. Y. Ivanov, D. M. Villeneuve, and P. B. Corkum, Measuring and controlling the birth of attosecond XUV pulses, Nat. Phys. **2**, 781 (2006).

[26] D. Shafir, H. Soifer, B. D. Bruner, M. Dagan, Y. Mairesse, S. Patchkovskii, M. Y. Ivanov, O. Smirnova, and N. Dudovich, Resolving the time when an electron exits a tunnelling barrier, Nature (London) **485**, 343 (2012).

[27] B. Ji, X. Song, Y. Dou, H. Tao, X. Gao, Z. Hao, and J. Lin, Two-color multiphoton emission for comprehensive reveal of ultrafast plasmonic field distribution, New J. Phys. **20**, 073031 (2018).

[28] G. Porat, G. Alon, S. Rozen, O. Pedatzur, M. Krüger, D. Azoury, A. Natan, G. Orenstein, B. D. Bruner, M. J. J. Vrakking, and N. Dudovich, Attosecond time-resolved photoelectron holography, Nat. Commun. **9**, 2805 (2018).

[29] M. Förster, T. Paschen, M. Krüger, C. Lemell, G. Wachter, F. Libisch, T. Madlener, J. Burgdörfer, and P. Hommelhoff, Two-Color Coherent Control of Femtosecond Above-Threshold Photoemission from a Tungsten Nanotip, Phys. Rev. Lett. **117**, 217601 (2016).

[30] T. Paschen, M. Förster, M. Krüger, C. Lemell, G. Wachter, F. Libisch, T. Madlener, J. Burgdörfer, and P. Hommelhoff, High visibility in two-color above-threshold photoemission from tungsten nanotips in a coherent control scheme, J. Mod. Opt. **64**, 1054 (2017).

[31] W. Cheng-Wei Huang, M. Becker, J. Beck, and H. Batelaan, Two-color multiphoton emission from nanotips, New J. Phys. **19**, 023011 (2017).

[32] Y. Luo and P. Zhang, Ultrafast strong-field photoelectron emission due to two-color laser fields, Phys. Rev. B **98**, 165442 (2018).

[33] Y. Luo and P. Zhang, Analysis of Two-Color Laser-Induced Electron Emission from a Biased Metal Surface Using an Exact Quantum Mechanical Solution, Phys. Rev. Applied **12**, 044056 (2019).

[34] E. W. Müller, Field ion microscopy, Science **149**, 591 (1965).

[35] S. Thomas, G. Wachter, C. Lemell, J. Burgdörfer, and P. Hommelhoff, Large optical field enhancement for nanotips with large opening angles, New J. Phys. **17**, 063010 (2015).

[36] S. Neppl, R. Ernstorfer, A. L. Cavalieri, C. Lemell, G. Wachter, E. Magerl, E. M. Bothschafter, M. Jobst, M. Hofstetter, U. Kleineberg, J. V. Barth, D. Menzel, J. Burgdörfer, P. Feulner, F. Krausz, and R. Kienberger, Direct observation of electron propagation and dielectric screening on the atomic length scale, Nature (London) **517**, 342 (2015).

[37] L. F. Mattheiss, Fermi surface in tungsten, Phys. Rev. **139**, A1893 (1965).

[38] See Supplemental Material at http://link.aps.org/supplemental/10.1103/PhysRevLett.126.137403 for more information on the field enhancement factors calculated for various wavelengths.

[39] U. Bovensiepen, H. Petek, and M. Wolf, *Dynamics at Solid State Surfaces and Interfaces* (Wiley-VCH Verlag GmbH & Co. KGaA, Weinheim, Germany, 2010).

[40] P. Dienstbier, T. Paschen, L. Seiffert, A. Liehl, A. Leitenstorfer, T. Fennel, and P. Hommelhoff (to be published).